Dalton Transactions

ROYAL SOCIETY OF CHEMISTRY

PAPER

View Article Online
View Journal | View Issue



Cite this: *Dalton Trans.*, 2024, **53**, 13364

# Multi-geometric carbon encapsulated $SnP_3$ composite for superior lithium/potassium ion batteries†

Zhongliang Hu,[a] Xixia Zhao, *[a,b] Yanqing Zhao,[a] Qian Zhao,[a] Xin Zhao, [a] Guijuan Wei*[a] and Honglei Chen*[a]

Received 3rd June 2024,
Accepted 19th July 2024

DOI: 10.1039/d4dt01616e

rsc.li/dalton



Tin phosphide has gained extensive attention as a prospective anode for lithium/potassium ion batteries because of its high theoretical capacity. Nevertheless, the fast capacity fading, which is induced by the huge volume expansion and poor electrical conductivity during cycling, severely restricts its practical applications. In this work, a $SnP_3$–CNTs/KB composite with a $SnP_3$ content as high as 90 wt% was successfully synthesized by a two-step ball milling method. $SnP_3$ nanoparticles were tightly encapsulated in multi-geometric composite carbon layers to efficiently relieve the volume changes and enhance conductivity. Specifically, the resulting $SnP_3$–CNTs/KB anode showed a specific capacity up to 998.6 mA h $g^{-1}$ after 100 cycles at 50 mA $g^{-1}$ and 810.4 mA h $g^{-1}$ after 500 cycles at 1000 mA $g^{-1}$ for lithium ion batteries. For potassium ion batteries, a high reversible capacity of 200.2 mA h $g^{-1}$ was achieved after 200 cycles at 1000 mA $g^{-1}$. This work affords a new insight for exploring excellent support structures of tin phosphide-based anodes.

## 1. Introduction

Lithium-ion batteries (LIBs) have been dominating the luggable energy storage field, but limited availability of lithium resources has increasingly turned out to be a major factor inhibiting the widespread use of LIBs.[1,2] Compared with LIBs, potassium-ion batteries (PIBs) have the potential to be used as low-cost and high-voltage batteries because of the abundant potassium resources and the low standard redox potential of potassium in a non-aqueous electrolyte, and therefore they are receiving increasing attention.[3,4] However, similar to LIBs, PIBs are faced with the problem of limited energy density and poor cycling performance of anode materials, which severely restricts their application.[5,6]

Among all types of anode materials for LIBs and PIBs, tin phosphides (*e.g.*, $Sn_4P_3$ and $SnP_3$) have high theoretical capacities comparable to phosphorus, but have relatively lower volume expansion due to the incorporation of tin, which is an emerging anode candidate for LIBs/PIBs.[7,8] Nevertheless, the inherent low electrical conductivity, coupled with huge volume expansion during alloying/de-alloying with lithium and potassium, results in rapid capacity degradation and inferior rate capability of pure tin phosphides.[9]

To enhance the performance of tin phosphides, many efforts have been devoted to alleviate volume expansion of tin phosphides and enhance electrode conductivity.[10–13] Current research mainly focuses on constructing tin phosphide–carbon composites, in which carbon not only improves the structural stability of tin phosphides but also provides convenient channels for electrons/ions.[14–16] Despite these advances, the dominant structure required to solve the two key problems of poor electrical conductivity and huge volume expansion of tin phosphide-based anodes to achieve the desired performance is not clear. Moreover, previous studies have mainly involved carbon support materials with a single-geometric structure, and few reports are available about the preparation of tin phosphide/carbon composites by combining various carbon materials with multi-geometric structures as support materials.

In this work, carbon nanotubes (CNTs) and Ketjen black (KB) were used to construct a multi-geometric composite carbon support for tin phosphide using a ball milling method. As the anode of LIBs, the $SnP_3$–CNTs/KB composite provided a high capacity of 810.4 mA h $g^{-1}$ after 500 cycles at

[a]*State Key Laboratory of Biobased Material and Green Papermaking, Key Laboratory of Pulp and Paper Science & Technology of Ministry of Education/Shandong Province, Faculty of Light Industry, Qilu University of Technology (Shandong Academy of Sciences), Jinan, 250353, P. R. China. E-mail: zhaoxixia163@163.com, weitiansd@126.com, chenhonglei_1982@163.com*
[b]*School of Chemistry and Chemical Engineering, University of Jinan, Jinan, 250022, P. R. China*

† Electronic supplementary information (ESI) available. See DOI: https://doi.org/10.1039/d4dt01616e

1000 mA $g^{-1}$. When used as the anode for PIBs, $SnP_3$–CNTs/KB exhibited a high specific capacity up to 200.2 mA h $g^{-1}$ after 200 cycles at 1000 mA $g^{-1}$.

## 2. Experimental

### 2.1. Chemicals

Red phosphorus (98.5%) was bought from Energy Chemicals. Tin particles (99.8%) were bought from 3A Chemicals. Multi-walled carbon nanotubes (CNTs, >95%) were bought from Aladdin. Ketjen black (KB, Carbon ECP) was bought from DodoChem.

### 2.2. Preparation of $SnP_3$ particles

$SnP_3$ particles were made by ball milling tin particles and red phosphorus under an argon atmosphere in a 1 : 3 molar ratio. A 20 : 1 weight ratio of milling balls to particles was used and the speed of the mill was set at 400 rpm for 40 h.

### 2.3. Preparation of the $SnP_3$–CNTs/KB composite

$SnP_3$ particles (90 wt%), CNTs (5 wt%) and KB (5 wt%) were milled under an argon atmosphere to prepare the $SnP_3$–CNTs/KB composite. A 20 : 1 weight ratio of milling balls to particles was used and the speed of the mill was set at 400 rpm for 24 h. The $SnP_3$–CNTs composite was made by milling $SnP_3$ particles (90 wt%) with CNTs (10 wt%), and the $SnP_3$–KB composite was made by milling $SnP_3$ particles (90 wt%) with KB (10 wt%).

### 2.4. Characterization

X-ray diffraction (XRD) patterns were recorded on an X-ray diffractometer (Rigaku SmartLab). Transmission electron microscopy (TEM) images were captured using a Tecnai F30 TEM system (300 kV). Scanning electron microscopy (SEM) images were obtained using a SEM system (Hitachi SU8010). X-ray photoelectron spectroscopy (XPS) spectra of materials were obtained with an XPS spectrometer (Thermo ESCALAB 250XI).

### 2.5. Electrochemical measurements

The electrochemical properties of the samples were evaluated by assembling CR2032 button half cells using 16 mm lithium discs or potassium discs as counter/reference electrodes. Copper foil was utilized as a collector and coated with a slurry of the active material and carboxymethyl cellulose in a weight ratio of 9 : 1. 12 mm diameter discs with a typical loading of 0.6–1.0 mg $cm^{-2}$ of the active material were used as working electrodes, and the battery capacity was calculated based on the mass of the active material. For LIBs, Celgard2325 acted as the separator, and 1.0 M $LiPF_6$ in EC/DMC (5% FEC) was used as the electrolyte. For PIBs, glass fiber acted as the separator, and 1.0 M KFSI in EC/DEC was used as the electrolyte. Cyclic voltammetry (CV) and discharge–charge tests were conducted within 0.01–3.0 V (*vs.* $Li^+$/Li) and 0.01–2.0 V (*vs.* $K^+$/K), respectively.

## 3. Results and discussion

The preparation process of the $SnP_3$–CNTs/KB composite is shown in Fig. 1. Tin and red phosphorus were first ball-milled to form $SnP_3$ nanoparticles. After further ball-milling with CNTs and KB, a dual-carbon conducting network structure was formed around the $SnP_3$ nanoparticles, in which the $SnP_3$ content was as high as 90 wt%. This structure not only favors the shortening of transport distances of ions and electrons, but also alleviates large volume changes during charging/discharging, thus boosting the rate and cycling performance.[17]

Fig. 2 depicts the XRD patterns of the as-synthesized composites, all of which fit well with the hexagonal structure of $SnP_3$ (JCPDS no. 72-0853). The main peaks at 21.9°, 24.1° and 32.8° belong to the (012), (110), and (202) planes of $SnP_3$, respectively, suggesting that the crystal structure of $SnP_3$ was not damaged during the milling process. However, characteristic peaks were not observed for CNTs or KB due to their low loading contents (10 wt%) and reduced crystallinity.

The morphologies of the composites are shown in Fig. 3a–c. Under the action of the shear force generated during the high-energy ball milling (HEBM) process, CNTs and KB achieved

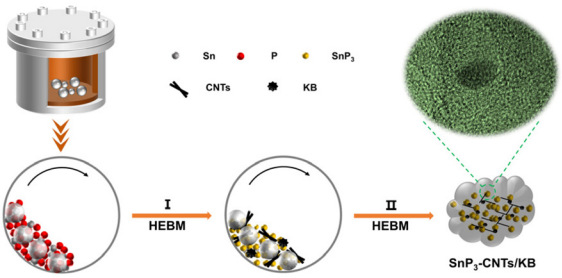


Fig. 1 Schematic diagram of the fabrication process of the $SnP_3$–CNTs/KB composite.

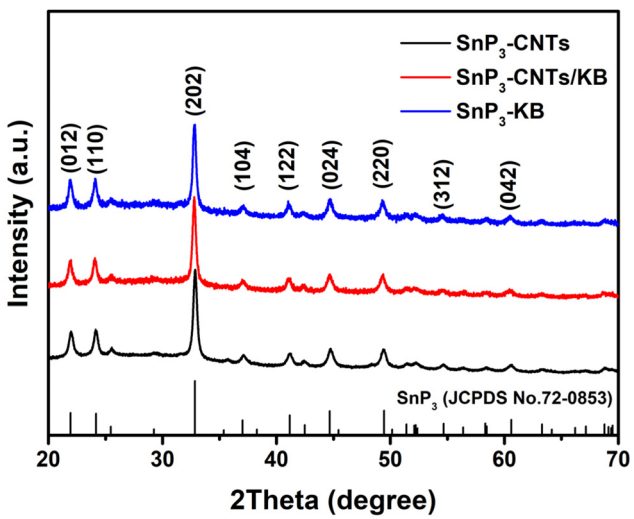


Fig. 2 XRD patterns of the as-synthesized composites.

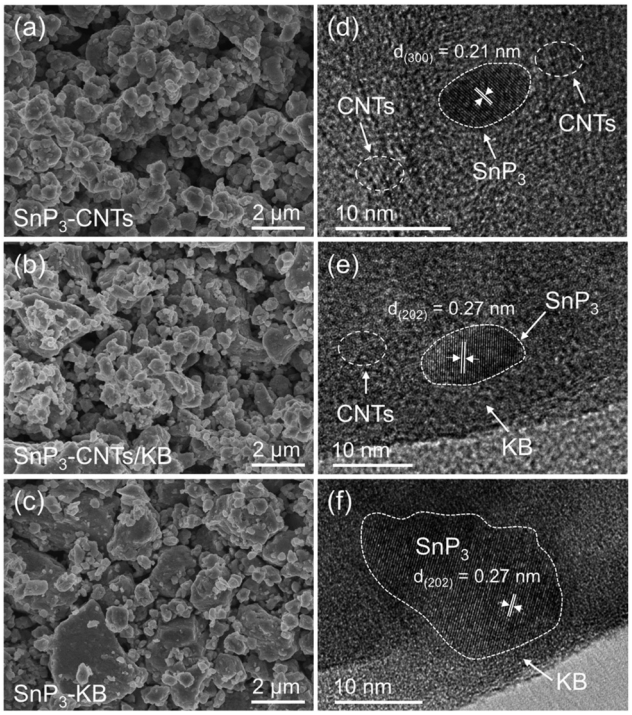


**Fig. 3** SEM and HRTEM images of the (a and d) $SnP_3$–CNTs, (b and e) $SnP_3$–CNTs/KB, and (c and f) $SnP_3$–KB composites.

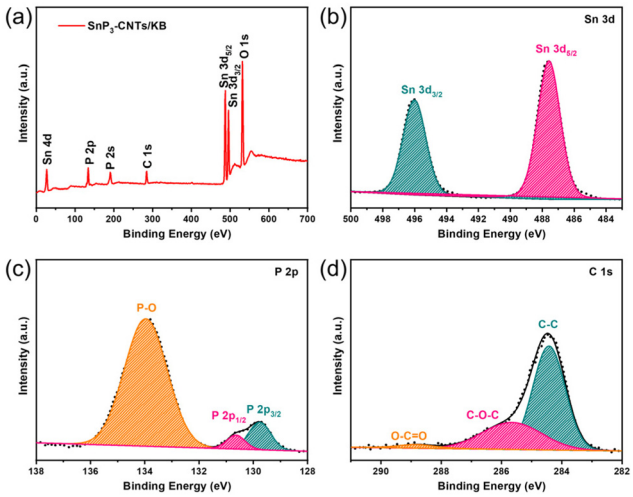


**Fig. 4** (a) Survey XPS spectrum and high-resolution XPS spectra of (b) Sn 3d, (c) P 2p, and (d) C 1s in the $SnP_3$–CNTs/KB composite.

homogeneous mixing with the $SnP_3$ particles. The HRTEM image displays an interplanar distance of 0.21 nm (Fig. 3d), corresponding to the (300) plane of $SnP_3$ (JCPDS no. 72-0853). In Fig. 3e and f, the interplanar distance of 0.27 nm can be indexed to the (202) plane of $SnP_3$.

Moreover, $SnP_3$ particles were surrounded by the CNTs/KB-formed multi-geometric network (Fig. 3e), beneficial for relieving the volume expansion of $SnP_3$ and promoting charge transfer during the charging/discharging process.[18] The obtained $SnP_3$–CNTs and $SnP_3$–KB composites exhibited structures similar to that of the $SnP_3$–CNTs/KB composite, but only with a single-geometric carbon structure.

The surface component and valence states of the $SnP_3$–CNTs/KB composite were investigated using XPS. Sn, P, O, and C elements were detected from the composite surface (Fig. 4a). For the high-resolution spectra of Sn 3d (Fig. 4b), 496.0 and 487.6 eV belong to Sn $3d_{3/2}$ and Sn $3d_{5/2}$, respectively.[19] For the P 2p spectrum (Fig. 4c), 130.6 and 129.8 eV are attributed to P $2p_{1/2}$ and P $2p_{3/2}$, respectively, while 133.9 eV is attributed to the phosphate species formed on the surface of $SnP_3$ when it was exposed to air. In Fig. 4d, 284.4, 285.7, and 288.8 eV are assigned to C–C, C–O–C, and O–C═O bonds, respectively.[20]

The surface areas and pore structures of the $SnP_3$–CNTs/KB composite, CNTs, and KB were studied through $N_2$ adsorption/desorption isotherms. It is observed from Fig. S1(a–c)† that all samples display a representative type-IV isothermal curve, revealing the mesoporous feature. The calculated BET surface areas and dominant pore diameters of the $SnP_3$–CNTs/KB composite, CNTs, and KB are 30.567 $m^2\ g^{-1}$ (3.86 nm), 184.468 $m^2\ g^{-1}$ (3.44 nm), and 810.815 $m^2\ g^{-1}$ (3.85 nm), respectively (Fig. S1(d–f)†). The porous structure and high specific surface area are conducive to providing more available channels for ion transport and rich active sites for ion insertion, thereby improving electrochemical lithium/potassium storage performance.

The electrochemical behavior of $SnP_3$ particles and the $SnP_3$–CNTs/KB composite as anodes for LIBs was investigated by CV in half cells. As shown in Fig. S2a,† reduction peaks at 0.3 and 0.7 V as well as oxidation peaks at 0.75 and 1.45 V were observed in the CV curves of $SnP_3$ particles, attributed to the reversible intercalation/conversion reactions:[21]

$$SnP_3 + xLi \leftrightarrow Li_xSnP_3\ (x \leq 4) \quad (1)$$

$$Li_xSnP_3\ (x \leq 4) + (13.25 - x)Li \leftrightarrow Li_{4.25}Sn + 3Li_3P \quad (2)$$

In subsequent cycles, the intensity of these redox peaks gradually decreased, indicating that the electrochemical reaction of pure $SnP_3$ particles is less reversible (Fig. S2a†). In contrast, these peaks of the $SnP_3$–CNTs/KB composite can be repeated and approximately overlapped after the first cycle (Fig. S2b†), showing greatly improved reversibility, which was also confirmed by its overlapped galvanostatic charge/discharge curves (Fig. S2c†).

Fig. 5a presents the rate performance of the $SnP_3$–CNTs/KB composite. Compared to $SnP_3$–CNTs and $SnP_3$–KB (Fig. S3†), the $SnP_3$–CNTs/KB composite electrode exhibited a superior rate capability and delivered capacities of 1230.5, 1086.3, 898.0, 804.9, and 715.2 mA h $g^{-1}$ at 50, 100, 200, 500, and 1000 mA $g^{-1}$, respectively. After 100 cycles at 50 mA $g^{-1}$ (Fig. 5b), the $SnP_3$–CNTs/KB composite electrode displayed a capacity as high as 998.6 mA h $g^{-1}$ with a coulombic efficiency close to 100%, higher than those of $SnP_3$–KB and $SnP_3$–CNTs (Fig. S4 and S5†). After 500 cycles at 1000 mA $g^{-1}$, the $SnP_3$–CNTs/KB electrode presented a specific capacity up to 810.4 mA h $g^{-1}$ (Fig. 5c). EIS Nyquist plots of the composites

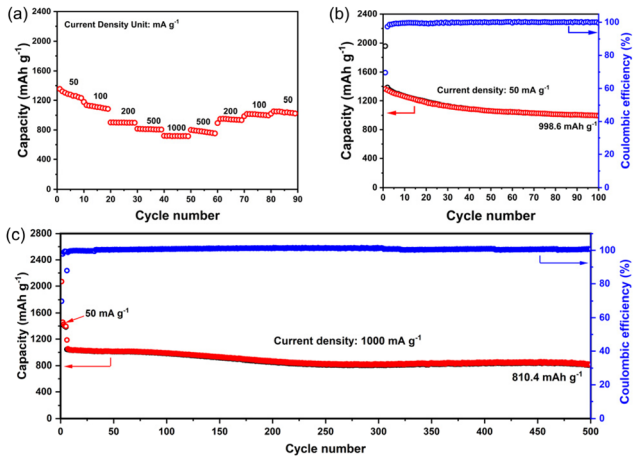


**Fig. 5** Electrochemical performance for LIBs: (a) rate performance of the $SnP_3$–CNTs/KB composite. (b) Cycling performance of the $SnP_3$–CNTs/KB composite at 50 mA $g^{-1}$. (c) Long-term cycling performance of the $SnP_3$–CNTs/KB composite at 1000 mA $g^{-1}$.

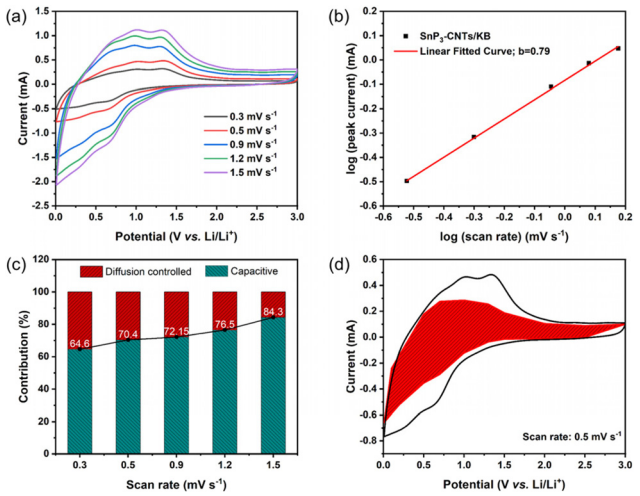


**Fig. 6** (a) CV curves of the $SnP_3$–CNTs/KB composite at different scan rates. (b) The *b* value obtained by plotting log *i* *vs.* log *v* lines. (c) Histograms of capacitive contribution to the total capacity of the $SnP_3$–CNTs/KB composite at different scan rates. (d) Illustration of charge contribution from capacitive and diffusion-controlled processes of the $SnP_3$–CNTs/KB composite at 0.5 mV $s^{-1}$.

are shown in Fig. S6.† It is obvious that $SnP_3$–CNTs/KB exhibited a smaller charge-transfer impedance ($R_{ct}$) than $SnP_3$–CNTs and $SnP_3$–KB, demonstrating the faster charge transfer kinetics of $SnP_3$–CNTs/KB. To our knowledge, the lithium storage capacity of the $SnP_3$–CNTs/KB electrode after long cycling is significantly higher than those of some tin phosphide-based anodes reported in the previous literature (Table 1).[20–28]

The pseudocapacitive charge storage and electrochemical transport kinetics of $SnP_3$–CNTs/KB were further explored by CV measurements with different sweep rates (Fig. 6a). The relationship between the peak current and scan rate can be calculated according to eqn (3) and (4).[29]

$$i = av^b \quad (3)$$

$$\log(i) = b\log(v) + \log(a) \quad (4)$$

$$i = k_1 v + k_2 v^{0.5} \quad (5)$$

In the equations, $i$ is the peak current, $v$ is the scan rate, and $a$ and $b$ are adjustable parameters. The pseudocapacitive contribution is further estimated quantitatively according to eqn (5),[29] where $k_1$ and $k_2$ are the adjustable parameters. In Fig. 6b, the calculated $b$ value corresponding to the anodic peak at ~1.32 V was about 0.79, indicating that the $SnP_3$–CNTs/KB electrode exhibited both pseudocapacitance and diffusion control behavior.[30]

Fig. 6c summarizes the pseudocapacitive contributions of $SnP_3$–CNTs/KB, which are 64.6%, 70.4%, 72.15%, 76.5%, and 84.3% at 0.3, 0.5, 0.9, 1.2, and 1.5 mV $s^{-1}$, respectively. Fig. 6d shows the detailed pseudocapacitive fraction of $SnP_3$–CNTs/KB compared to the whole current at 0.5 mV $s^{-1}$. Therefore, the contribution of pseudocapacitance may be part of the reason for the outstanding electrochemical performance of $SnP_3$–CNTs/KB electrodes.

The electrochemical properties of the $SnP_3$–CNTs, $SnP_3$–CNTs/KB, and $SnP_3$–KB composites as anodes for PIBs were tested in half cells. The storage behavior of potassium ions was evaluated by CV. As shown in Fig. S7,† a major peak at around 0.01 V was observed in the initial cathodic scan. In the anodic scan, a broad peak centered at 0.75 and a weak peak at 1.4 V can be observed, assigned to the depotassiation processes of K–Sn/K–P.[31] Fig. 7a presents the rate performance of the composites. Compared to $SnP_3$–CNTs and $SnP_3$–KB, the $SnP_3$–CNTs/KB composite electrode exhibited a superior rate capability and delivered capacities of 395.3, 386.5, 332.2, 281.6, and 220.2 mA h $g^{-1}$ at 50, 100, 200, 500, and 1000 mA $g^{-1}$, respectively. The initial charge/discharge voltage profiles of the composites at 50 mA $g^{-1}$ are depicted in Fig. 7b. After 200 cycles at 1000 mA $g^{-1}$, the $SnP_3$–CNTs/KB electrode displayed a specific capacity up to 200.2 mA h $g^{-1}$ (Fig. 7c).

Fig. 7d shows the initial coulombic efficiency (ICE) of the composites at 1000 mA $g^{-1}$. The ICE values of the $SnP_3$–CNTs,

**Table 1** Summary of cycling performances of some tin phosphides for LIBs

| Materials | Current density (mA $g^{-1}$) | Cycle number | Capacity (mA h $g^{-1}$) | Ref. |
|---|---|---|---|---|
| $Sn_4P_3$–NC | 1000 | 400 | 506.9 | 22 |
| SnP/C | 1000 | 500 | 610 | 23 |
| $Sn_4P_3$/C | 200 | 100 | 727 | 23 |
| MWCNTs/$Sn_4P_3$@C | 1000 | 1000 | 569.5 | 24 |
| $Sn_4P_3$/C composite | 1000 | 400 | 760 | 20 |
| $SnP_3$/C | 100 | 100 | 395 | 21 |
| $Sn_4P_3$ nanoparticles | 1000 | 90 | 207 | 25 |
| Mn-doped $Sn_4P_3$ | 1000 | 200 | 255 | 26 |
| $Sn_3P_4$/$Sn_4P_3$@C | 1000 | 100 | 513 | 27 |
| $Sn_xP_y$/C-2 | 1000 | 300 | 366 | 28 |
| $SnP_3$–CNTs/KB | 1000 | 500 | 810.4 | This work |

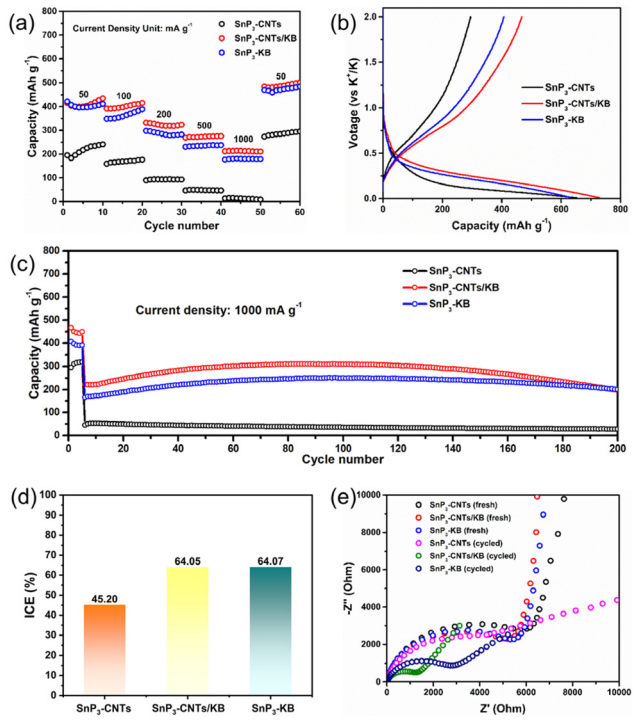


**Fig. 7** Electrochemical performance for PIBs: (a) rate performances of the composites. (b) Initial charge/discharge voltage profiles of the composites at 50 mA $g^{-1}$. (c) Long-term cycling performances of the composites at 1000 mA $g^{-1}$. (d) Comparison of the initial coulombic efficiency (ICE) of the composites at 1000 mA $g^{-1}$. (e) EIS Nyquist plots of the $SnP_3$–CNTs, $SnP_3$–CNTs/KB, and $SnP_3$–KB composites before and after 200 cycles.

$SnP_3$–CNTs/KB, and $SnP_3$–KB composites are 45.20%, 64.05%, and 64.07%, respectively. EIS Nyquist plots of the composites before and after 200 cycles are shown in Fig. 7e. The $R_{ct}$ values of $SnP_3$–CNTs/KB both before and after cycling are significantly lower than those of the other two electrodes. As displayed in Table 2, the reversible capacity of $SnP_3$–CNTs/KB after long cycling at a high current density is higher than those of most previously reported tin phosphide-based anodes for PIBs.[15,16,31–38]

**Table 2** Summary of cycling performances of some tin phosphides for PIBs

| Materials | Current density (mA $g^{-1}$) | Cycle number | Capacity (mA h $g^{-1}$) | Ref. |
|---|---|---|---|---|
| $Sn_4P_3$/C | 50 | 50 | 307.2 | 31 |
| $Sn_4P_3$@carbon fiber | 500 | 1000 | 160.7 | 32 |
| $Sn_4P_3$/RGO | 600 | 60 | 156 | 33 |
| $Sn_4P_3$@C | 500 | 800 | 181.5 | 34 |
| $SnP_{0.94}$@GO | 200 | 100 | 106 | 15 |
| $SnP_3$/C | 500 | 80 | 225 | 35 |
| r-SnP@C | 1000 | 200 | 235.9 | 36 |
| T-SnP | 500 | 180 | 298.2 | 37 |
| $SnP_3$/CNTs-20 | 1000 | 150 | 190 | 16 |
| $SnP_3$–CNTs/KB | 1000 | 200 | 200.2 | This work |

Based on all the above-mentioned results, the $SnP_3$–CNTs/KB composite used as anodes displayed better lithium/potassium storage performance than the $SnP_3$–KB and $SnP_3$–CNTs composites, which mainly depends on the multi-geometric design of the composite carbon support. The high surface area of KB could enable a uniform distribution and tight encapsulation of $SnP_3$ particles, while the high conductivity of KB and CNTs yielded a dual conductive network in the $SnP_3$–CNTs/KB composite. Such a unique structure could greatly enhance the electronic conductivity and increase the mechanical strength of the composite, and hence improve its rate performance and prolong its cycle life. The attractive lithium/potassium storage properties of the $SnP_3$–CNTs/KB composite demonstrate its wide range of applications.

## Conclusions

The $SnP_3$–CNTs/KB composite with a $SnP_3$ content as high as 90 wt% was successfully synthesized by a two-step HEBM method, which delivered a high reversible capacity of 998.6 mA h $g^{-1}$ over 100 cycles at 50 mA $g^{-1}$ and 810.4 mA h $g^{-1}$ even after 500 cycles at 1000 mA $g^{-1}$ for LIBs. Moreover, the achieved capacities of $SnP_3$–CNTs/KB for PIBs, especially at high current densities, are better than those of most other reported tin phosphide anodes. These results might be attributed to the multi-geometric structure of the carbon support in the composite, which is not only beneficial for reducing the transfer distance of ions and electrons, but also can relieve large volume expansion during the charging/discharging process. This study affords a new insight for enhancing the performance of tin phosphide-based anodes.

## Author contributions

Zhongliang Hu: data curation, formal analysis, and writing – original draft; Xixia Zhao: conceptualization, funding acquisition, methodology, supervision, and writing – review & editing; Yanqing Zhao: data curation and investigation; Qian Zhao: funding acquisition and supervision; Xin Zhao: funding acquisition and supervision; Guijuan Wei: funding acquisition, supervision, and writing – review & editing; Honglei Chen: funding acquisition, supervision, and writing – review & editing.

## Data availability

The data that support the findings of this study are available from the corresponding author upon reasonable request.

## Conflicts of interest

The authors declare no conflict of interest associated with this article.

## Acknowledgements

This work was supported by the National Natural Science Foundation of China (No. 32271802, 32271801, 52102269), the Shandong Provincial Natural Science Foundation (No. ZR2022MC190, ZR2023QB015), the Pilot Project for Integrating Science, Education and Industry from Qilu University of Technology, Shandong Academy of Sciences (No. 2023PYI003, 2023PX005, 2023PX009), the QUTJBZ Program (No. 2022JBZ01-05), and the Talent Research Project from Qilu University of Technology, Shandong Academy of Sciences (No. 2023RCKY187, 2023RCKY198).

## References

1 P. Xu, D. H. S. Tan, B. Jiao, H. Gao, X. Yu and Z. Chen, *Adv. Funct. Mater.*, 2023, **33**, 2213168.
2 J. Wu, M. Zheng, T. Liu, Y. Wang, Y. Liu, J. Nai, L. Zhang, S. Zhang and X. Tao, *Energy Storage Mater.*, 2023, **54**, 120–134.
3 J. Zheng, C. Hu, L. Nie, H. Chen, S. Zang, M. Ma and Q. Lai, *Adv. Mater. Technol.*, 2023, **8**, 2201591.
4 K. Sada, J. Darga and A. Manthiram, *Adv. Energy Mater.*, 2023, **13**, 2302321.
5 G. Luo, X. Feng, M. Qian, W. Zhang, W. Qin, C. Wu and L. Pan, *Mater. Chem. Front.*, 2023, **7**, 3011–3036.
6 W. Zhang, R. Huang, X. Yan, C. Tian, Y. Xiao, Z. Lin, L. Dai, Z. Guo and L. Chai, *Angew. Chem., Int. Ed.*, 2023, **62**, e202308891.
7 K. I. Dhanalekshmi, P. Magesan, X. Ma, X. Zhang and K. Jayamoorthy, *J. Energy Storage*, 2023, **68**, 107691.
8 S. Dong, L. Wang, X. Huang, J. Liang and X. He, *Batteries Supercaps*, 2023, **6**, e202300265.
9 J. Zhang and J. Zhao, *J. Energy Storage*, 2023, **72**, 108366.
10 Z. Kong, Z. Liang, M. Huang, H. Tu, K. Zhang, Y. Shao, Y. Wu and X. Hao, *J. Alloys Compd.*, 2023, **930**, 167328.
11 L. Wang, Q. Li, Z. Chen, Y. Wang, Y. Li, J. Chai, N. Han, B. Tang, Y. Rui and L. Jiang, *Small*, 2024, 2310426.
12 R. He, X. Wang, J. Li, L. Chang, H. Wang and P. Nie, *Appl. Surf. Sci.*, 2024, **654**, 159532.
13 A. Belgibayeva, M. Rakhatkyzy, A. Rakhmetova, G. Kalimuldina, A. Nurpeissova and Z. Bakenov, *Small*, 2023, **19**, 2304062.
14 L. Yue, J. Liang, Z. Wu, B. Zhong, Y. Luo, Q. Liu, T. Li, Q. Kong, Y. Liu, A. M. Asiri, X. Guo and X. Sun, *J. Mater. Chem. A*, 2021, **9**, 11879–11907.
15 X. Zhao, W. Wang, Z. Hou, G. Wei, Y. Yu, J. Zhang and Z. Quan, *Chem. Eng. J.*, 2019, **370**, 677–683.
16 X. Zhao, X. Yu, G. Wei, F. Kong and W. Wang, *Compos. Commun.*, 2021, **28**, 100938.
17 J. Ruan, J. Zang, J. Hu, R. Che, F. Fang, F. Wang, Y. Song and D. Sun, *Adv. Sci.*, 2022, **9**, 2104822.
18 X. Li, H. Liang, X. Liu, R. Sun, Z. Qin, H. Fan and Y. Zhang, *Chem. Eng. J.*, 2021, **425**, 130657.
19 E. Pan, Y. Jin, C. Zhao, M. Jia, Q. Chang and M. Jia, *J. Alloys Compd.*, 2018, **769**, 45–52.
20 Z. Liu, X. Wang, Z. Wu, S. Yang, S. Yang, S. Chen, X. Wu, X. Chang, P. Yang, J. Zheng and X. Li, *Nano Res.*, 2020, **13**, 3157–3164.
21 J.-W. Park and C.-M. Park, *Sci. Rep.*, 2016, **6**, 35980.
22 Z. Liu, J. Chen, X. Fan, Y. Pan, Y. Li, L. Ma, H. Zhai and L. Xu, *J. Alloys Compd.*, 2021, **871**, 159531.
23 M. Wang, G.-M. Weng, G. Yasin, M. Kumar and W. Zhao, *Dalton Trans.*, 2020, **49**, 17026–17032.
24 S. Sun, R. Li, W. Wang, D. Mu, J. Liu, T. Chen, S. Tian, W. Zhu and C. Dai, *Inorg. Chem. Front.*, 2020, **7**, 2651–2659.
25 S. Liu, H. Zhang, L. Xu, L. Ma and X. Chen, *J. Power Sources*, 2016, **304**, 346–353.
26 S. Liu, H. Zhang, L. Xu, L. Ma and X. Hou, *Electrochim. Acta*, 2016, **210**, 888–896.
27 Q. Liu, C. Liu, Z. Li, Q. Liang, B. Zhu, J. Chai, X. Cheng, P. Zheng, Y. Zheng and Z. Liu, *ACS Appl. Energy Mater.*, 2021, **4**, 11306–11313.
28 M. Zhang, H. Wang, J. Feng, Y. Chai, X. Luo, R. Yuan and X. Yang, *Appl. Surf. Sci.*, 2019, **484**, 899–905.
29 V. Augustyn, J. Come, M. A. Lowe, J. W. Kim, P.-L. Taberna, S. H. Tolbert, H. D. Abruña, P. Simon and B. Dunn, *Nat. Mater.*, 2013, **12**, 518–522.
30 H.-S. Kim, J. B. Cook, H. Lin, J. S. Ko, S. H. Tolbert, V. Ozolins and B. Dunn, *Nat. Mater.*, 2017, **16**, 454–460.
31 W. Zhang, J. Mao, S. Li, Z. Chen and Z. Guo, *J. Am. Chem. Soc.*, 2017, **139**, 3316–3319.
32 W. Zhang, W. K. Pang, V. Sencadas and Z. Guo, *Joule*, 2018, **2**, 1534–1547.
33 W. Yang, J. Zhang, D. Huo, S. Sun, S. Tao, Z. Wang, J. Wang, D. Wu and B. Qian, *Ionics*, 2019, **25**, 4795–4803.
34 D. Li, Y. Zhang, Q. Sun, S. Zhang, Z. Wang, Z. Liang, P. Si and L. Ci, *Energy Storage Mater.*, 2019, **23**, 367–374.
35 R. Verma, P. N. Didwal, H.-S. Ki, G. Cao and C.-J. Park, *ACS Appl. Mater. Interfaces*, 2019, **11**, 26976–26984.
36 B. Li, S. Shang, J. Zhao, D. M. Itkis, X. Jiao, C. Zhang, Z.-K. Liu and J. Song, *Carbon*, 2020, **168**, 468–474.
37 C.-Y. Tsai, C.-H. Chang, T.-L. Kao, K.-T. Chen and H.-Y. Tuan, *Chem. Eng. J.*, 2021, **417**, 128552.
38 J. Zhao, C. Li, G. Chen, F. Ji, Y. Shen, J. Peng and W. Wang, *Rare Met.*, 2022, **41**, 2259–2267.